

Shape of the acoustic gravitational wave power spectrum from a first order phase transition

Mark Hindmarsh,^{1,2,*} Stephan J. Huber,^{1,†} Kari Rummukainen,^{2,‡} and David J. Weir^{2,§}

¹*Department of Physics and Astronomy, University of Sussex, Falmer, Brighton BN1 9QH, U.K.*

²*Department of Physics and Helsinki Institute of Physics, PL 64, FI-00014 University of Helsinki, Finland*

(Dated: April 20, 2017)

We present results from large-scale numerical simulations of a first order thermal phase transition in the early universe, in order to explore the shape of the acoustic gravitational wave and the velocity power spectra. We compare the results with the predictions of the recently proposed sound shell model. For the gravitational wave power spectrum, we find that the predicted k^{-3} behaviour, where k is the wavenumber, emerges clearly for detonations. The power spectra from deflagrations show similar features, but exhibit a steeper high- k decay and an extra feature not accounted for in the model. There are two independent length scales: the mean bubble separation and the thickness of the sound shell around the expanding bubble of the low temperature phase. It is the sound shell thickness which sets the position of the peak of the power spectrum. The low wavenumber behaviour of the velocity power spectrum is consistent with a causal k^3 , except for the thinnest sound shell, where it is steeper. We present parameters for a simple broken power law fit to the gravitational wave power spectrum for wall speeds well away from the speed of sound where this form can be usefully applied. We examine the prospects for the detection, showing that a LISA-like mission has the sensitivity to detect a gravitational wave signal from sound waves with an RMS fluid velocity of about $0.05c$, produced from bubbles with a mean separation of about 10^{-2} of the Hubble radius. The shape of the gravitational wave power spectrum depends on the bubble wall speed, and it may be possible to estimate the wall speed, and constrain other phase transition parameters, with an accurate measurement of a stochastic gravitational wave background.

I. INTRODUCTION

The first direct observation of gravitational waves by LIGO in 2015 has opened a new and unexplored window to the cosmos [1, 2]. Even more excitingly, while the original detection was related to an astrophysical process, the merger of two black holes, gravitational waves will also allow us to directly probe processes in the very early universe, such as inflation [3], topological defects [4–7] and first order phase transitions [8]. To study gravitational wave signals from these and other sources the space-based gravitational wave observatory LISA is due to launch about a decade from now [9]. The LISA Pathfinder mission has recently demonstrated the technological feasibility of such a mission [10].

LISA will have particular sensitivity in the millihertz frequency range, making it an ideal instrument to observe gravitational wave signals from phase transitions in the electroweak era, corresponding to roughly 10 picoseconds after the big bang. First order phase transitions proceed via the nucleation, expansion, collision and merger of bubbles of the low temperature (broken) phase. They can source gravitational waves in a number of ways. Firstly, gravitational radiation is produced by the collisions of the bubble walls, where the scalar order parameter changes from the symmetric to the broken phase. If

the phase transition occurred in vacuum, this would be the only source of gravitational waves. The energy momentum tensor of this source is well approximated by the envelope of a configuration of infinitely thin shells [11–13]; this is known as the envelope approximation [14]. It leads to a characteristic high-wavenumber (UV) fall-off of the spectrum proportional to k^{-1} , where k is the wave number, which has been recently confirmed by both numerical simulations [15] and analytic modelling [16].

If the scalar bubbles expand in a hot plasma, as expected to be the case in the early universe, friction from the plasma will slow down the walls, which after initial acceleration will expand with a constant speed v_w . In this case most energy released by the transition will be transferred from the scalar field into the plasma. Only a tiny fraction, on the order of microphysics scale to bubble radius at collision, will remain in the scalar field. So the scalar field source is completely negligible for a thermal cosmological phase transition¹. The energy transferred to the medium can either go to heat or fluid motion. Numerical simulations show that the energy momentum tensor of the fluid after bubble collisions corresponds to an ensemble of sound waves. These sound waves in turn are an efficient source of gravitational radiation [19–21].

¹ According to Ref. [17] for very strong thermal transitions, friction from the plasma will not stop the bubbles from accelerating towards the speed of light (“runaway bubbles”). However, it is expected that additional friction from higher order corrections related to particle production will modify this result [18]. So runaway bubbles are expected to correspond to very fast standard detonations.

* m.b.hindmarsh@sussex.ac.uk

† s.huber@sussex.ac.uk

‡ kari.rummukainen@helsinki.fi

§ david.weir@helsinki.fi

An analytical model of the velocity perturbations in this acoustic phase of the transition based on a picture of the acoustic phase fluctuations as overlapping shells of sound waves has recently been proposed [22], in which the UV fall-off of the spectrum is roughly k^{-3} , so distinctly different from the transition in the vacuum case. This means that an observation of such a gravitational wave signal with LISA could allow to distinguish between the two cases, such giving valuable information on the nature of the transition. For very strong transitions it is expected that the acoustic phase turns over into a turbulent stage [23–29]. This turbulence will continue to produce gravitational radiation until it decays.

In this paper we present results from extensive numerical simulations, building on earlier work reported in Refs. [20, 21]. We model the system by a scalar order parameter field coupled to a relativistic fluid by means of a phenomenological friction term. The resulting Klein-Gordon equation coupled to relativistic hydro-dynamics is solved on a lattice. We use it to study the acoustic phase at an unprecedented level of accuracy.

We show detailed velocity and gravitational wave power spectra, for both deflagrations and detonations, and compare them to the predictions of the sound shell model. The UV power laws agree with the model in the case of detonations, and the prediction of an intermediate k^1 power law for wall speeds close to the speed of sound is also corroborated. We establish that there are two length scales in the power spectrum: the mean bubble separation, and the width of the sound pulse around the expanding bubble wall, the “shell” of the sound shell model. The UV power law for deflagrations is steeper than the model prediction, with an interesting break or knee.

We show that the gravitational wave power spectrum for wall speeds well away from the speed of sound can be modelled with a broken power law and an amplitude proportional to the fourth power of the RMS fluid velocity and to the ratio of the fluid flow length scale to the Hubble length. We use the model to forecast the sensitivity of LISA [9] to acoustically generated gravitational waves.

Characterising the fluid flow length scale by the mean bubble separation, we find that the peak sensitivity is to transitions with a mean bubble separation of order 10^{-2} of the Hubble length at a transition with critical temperature 10^2 GeV. Transitions generating an RMS fluid velocity of about 0.05 (in natural units) give rise to acoustic gravitational waves with signal-to-noise ratio of about 10.

We also estimate the timescale on which the acoustic waves become shocked due to non-linear evolution, which would cause the velocity and gravitational wave power spectra to deviate from their acoustic form. A significant part of the parameter space generating observable gravitational waves is likely to feature shocks and eventually turbulence, for which further simulation is required to establish an accurate power spectrum.

When interfaced with a particular microphysics realisation of a phase transition to provide the main input parameters, latent heat, bubble size and wall velocity, our results allow accurate estimations of the resulting gravitational wave signal. Conversely, the differences in the shapes we observe point the way towards estimating the wall speed and constraining combinations of other phase transition parameters from accurate observations of a primordial gravitational wave power spectrum.

In the following section we recap the physics of the acoustic generation of gravitational waves after a first-order thermal phase transition; in Section III we discuss our numerical methods, highlighting aspects of our approach which differ from Refs. [20, 21]; our results for the fluid velocity power spectrum can be found in Section IV and for gravitational waves in Section V. We then compare these results to the power law ansatz used for the LISA Cosmology Working Group report (Ref. [8]) in Section VI. Our conclusions are in Section VII.

II. ACOUSTIC GRAVITATIONAL WAVES

The source of the gravitational waves is shear stress in the system, induced by the nucleation, explosive growth and merger of bubbles of the Higgs phase. These perturbations take the form of compression and rarefaction waves laid down around the growing bubbles - that is, the sound of the Higgs explosions.

A. Thermodynamics

The sources of shear stress are the order parameter ϕ and the relativistic fluid to which it is coupled. Because we need only the transverse-traceless part of the energy-momentum tensor, it is sufficient to consider as a source tensor $\tau_{ij} = \tau_{ij}^\phi + \tau_{ij}^f$, which is decomposed into fluid and field pieces according to

$$\tau_{ij}^\phi = \partial_i \phi \partial_j \phi, \quad \tau_{ij}^f = W^2 w V_i V_j, \quad (1)$$

where $w = \epsilon + p$ is the enthalpy density, ϵ is the energy density, p is the pressure, V_i is the fluid 3-velocity, and W is the corresponding Lorentz factor. Unless the transition is strongly supercooled, most of the available energy of the transition goes into thermal and kinetic energy of the fluid; the scalar contribution is negligible.

It is useful to describe the overall amplitude of the fluid shear stress by a root mean square (RMS) four-velocity \bar{U}_f defined through

$$\bar{U}_f^2 = \frac{1}{\bar{w}\mathcal{V}} \int_{\mathcal{V}} d^3x \tau_{ii}^f, \quad (2)$$

where \mathcal{V} is the averaging volume and \bar{w} is the volume averaged enthalpy density. One can define a similar quantity for the scalar field

$$\bar{U}_\phi^2 = \frac{1}{\bar{w}\mathcal{V}} \int_{\mathcal{V}} d^3x \tau_{ii}^\phi. \quad (3)$$

Although these are not quite the magnitudes of the transverse traceless part of the shear stress, they are easy to compute, and do have a direct connection to the gravitational wave amplitude for random fields, as we shall see in Eq. (21).

The fluid energy density and pressure have a contribution from the scalar order parameter of the phase transition ϕ , through its effective potential $V(\phi, T)$,

$$p(T, \phi) = \frac{\pi^2}{90} g_* T^4 - V(\phi, T) \quad (4)$$

$$\epsilon(T, \phi) = \frac{\pi^2}{30} g_* T^4 + V(\phi, T) - T \frac{\partial V}{\partial T}, \quad (5)$$

where g_* is the effective number of relativistic degrees of freedom.

Following [30, 31], we use a simple quartic form for the potential:

$$V(\phi, T) = \frac{1}{2} \gamma (T^2 - T_0^2) \phi^2 - \frac{1}{3} A T \phi^3 + \frac{1}{4} \lambda \phi^4. \quad (6)$$

The detailed form is not important: its function is to supply a metastable state with a latent heat

$$\mathcal{L}(T) = w(T, 0) - w(T, \phi_b) \quad (7)$$

where ϕ_b is the equilibrium value of the field in the symmetry-broken phase at temperature T . The strength of the transition can be parametrised by the ratio of the latent heat to the total radiation density in the high temperature symmetric phase²

$$\alpha_w = \frac{\mathcal{L}(T)}{\epsilon_r(T)}. \quad (8)$$

A commonly used alternative is the difference in the trace anomaly divided by a conventional factor of 4, or

$$\Delta\theta(T) = -\frac{T}{4} \frac{d}{dT} \Delta V + \Delta V, \quad (9)$$

where $\Delta V(T) = V(0, T) - V(\phi_b, T)$. Expressed relative to the energy density in the symmetric phase

$$\alpha_\theta = \frac{\Delta\theta(T)}{\epsilon_r(T)}. \quad (10)$$

Other important parameters are the surface tension and width of the phase boundary σ and ℓ , which can be computed straightforwardly from the parameters of the potential [21, 30]. The transition takes place at the nucleation temperature T_n , at which the radius of the critical bubble is denoted R_c .

B. Shear stress and velocity correlations

As mentioned above, the dominant source of shear stress is the fluid, unless $\alpha \gg 1$ by the measures of the phase transition strength outlined above, and the scalar field is so weakly coupled with the fluid that the walls continue to accelerate until collision. Our simulations explore the more generic situation, $\alpha \lesssim 1$.

One can characterise the fluid source by the unequal time correlator (UETC) of the shear stress Π^2 [33, 34], defined by projecting out the spatially transverse and traceless part of the energy-momentum tensor

$$\lambda_{ij,kl}(\mathbf{k}) \left\langle \tau_{\mathbf{f}}^{ij}(\mathbf{k}, t_1) \tau_{\mathbf{f}}^{kl}(\mathbf{k}', t_2) \right\rangle = \Pi^2(k, t_1, t_2) (2\pi)^3 \delta(\mathbf{k} + \mathbf{k}'), \quad (11)$$

where

$$\lambda_{ij,kl}(\mathbf{k}) = P_{ik}(\mathbf{k}) P_{jl}(\mathbf{k}) - \frac{1}{2} P_{ij}(\mathbf{k}) P_{kl}(\mathbf{k}) \quad (12)$$

and

$$P_{ij}(\mathbf{k}) = \delta_{ij} - \hat{k}_i \hat{k}_j. \quad (13)$$

The shear stresses are the result of the sound waves, which can be characterised by the longitudinal part of the velocity unequal time correlator $G(q, t_1, t_2)$. This is defined from the Fourier transform of the velocity field $\tilde{v}_{\mathbf{q}_1}^i$ through

$$\hat{q}^i \hat{q}^j \left\langle \tilde{v}_{\mathbf{q}_1}^i(t_1) \tilde{v}_{\mathbf{q}_2}^{*j}(t_2) \right\rangle = G(q, t_1, t_2) (2\pi)^3 \delta(\mathbf{q}_1 - \mathbf{q}_2). \quad (14)$$

The transverse part G^\perp can be defined analogously. We will be interested in the velocity power spectrum,

$$\frac{dV^2}{d\ln(q)} = \frac{q^3}{2\pi^2} (G(q, t, t) + G^\perp(q, t, t)). \quad (15)$$

In our simulations, the longitudinal part is always much greater than the transverse part (see Table III), reflecting the dominance of sound waves in the fluid perturbations.

C. Gravitational waves

The transverse traceless metric perturbation h_{ij} is extracted by projection from an auxiliary tensor u_{ij} satisfying the equation

$$\square u_{ij} = (16\pi G) \tau_{ij}^f \quad (16)$$

The energy density in gravitational waves is

$$\rho_{\text{gw}} = \frac{1}{32\pi G} \left\langle \dot{h}_{ij} \dot{h}_{ij} \right\rangle, \quad (17)$$

where h_{ij} is the transverse-traceless projection of u_{ij} . It is most useful to consider the gravitational wave power spectrum relative to the critical density, defined as

$$\frac{d\Omega_{\text{gw}}}{d\ln(k)} = \frac{1}{12H^2} \frac{k^3}{2\pi^2} P_h(\mathbf{k}, t), \quad (18)$$

² Note that the radiation density has no unique definition in a system with a scalar order parameter in a thermal bath: here we follow Ref. [32] and define it as $\epsilon_r(T) = 3w(T, 0)/4$.

where H is the Hubble parameter and P_h is the power spectral density, defined from the two-point correlation

$$\langle \dot{h}_{ij}(\mathbf{k}, t) \dot{h}_{ij}(\mathbf{k}', t) \rangle = P_h(\mathbf{k}, t) (2\pi)^3 \delta(\mathbf{k} + \mathbf{k}'). \quad (19)$$

In our simulations, the expansion of the universe is scaled out using the scale invariance of the relativistic fluid equations [21, 35]. Nonetheless, one can still formally compute the Hubble rate from the Friedmann equation

$$H^2 = \frac{8\pi G}{3} \epsilon(0, T). \quad (20)$$

It was shown in Ref. [21] that, after the acoustic source has been on for time t , the dimensionless gravitational wave power spectrum takes the form

$$\frac{d\Omega_{\text{gw}}(k)}{d\ln(k)} = 3\Gamma^2 \bar{U}_f^4 (H_n t) (H_n L_f) \frac{(k L_f)^3}{2\pi^2} \tilde{P}_{\text{gw}}(k L_f), \quad (21)$$

where $\Gamma = 1 + \bar{p}/\bar{\epsilon}$ is the adiabatic index, \bar{U}_f is the RMS fluid velocity, H_n is the Hubble rate at the bubble nucleation temperature T_n , L_f is the characteristic length of the fluid flow, and \tilde{P}_{gw} is a dimensionless spectral density for the gravitational waves.

It was also shown that, provided that turbulence does not develop within a Hubble time, the effective time for which the acoustic source operates is precisely the Hubble time, so that $H_n t \rightarrow 1$.

The turbulence timescale, both for appearance and decay, is the shock appearance or eddy turn-over time [36, 37]

$$\tau_{\text{sh}} \sim L_f / \bar{U}_f. \quad (22)$$

The maximum duration of all our simulations is much less than τ_{sh} , and so no turbulence develops. Our results therefore apply to flows for which $\bar{U}_f \ll L_f H_*$.

In the acoustic phase the total gravitational wave energy density grows as

$$\Omega_{\text{gw}} = 3\Gamma^2 \bar{U}_f^4 (H_n t) (H_n L_f) \tilde{\Omega}_{\text{gw}}, \quad (23)$$

where

$$\tilde{\Omega}_{\text{gw}} = \frac{1}{2\pi^2} \int_0^\infty dx x^2 \tilde{P}_{\text{gw}}(x) \quad (24)$$

is a dimensionless parameter, quantifying the efficiency with which shear stress is converted to gravitational waves. A significant result in [21] was that this parameter is approximately independent of the length scale and RMS velocity of the fluid flow.

III. METHODS

The system is a set of coupled partial differential equations governing the evolution of the scalar field ϕ

Parameter	Weak	Intermediate
g_*	106.75	106.75
T_0/T_c	$1/\sqrt{2}$	$1/\sqrt{2}$
γ	2/9	4/9
A	0.1990	0.1990
λ	0.0792	0.0396
T_n/T_c	0.86	0.80
\mathcal{L}/T_c^4	0.7013	5.6102
σ/T_c^3	0.1558	0.8816
ℓT_c	3	2.1213
$\phi_b(T_n)/T_c$	1.7838	3.5810
$\alpha_w(T_n)$	0.010	0.084
$\alpha_\theta(T_n)$	0.0046	0.050
v_{CJ}	0.63	0.73
$R_c T_c$	8.1	4.3
$H_n/\sqrt{G}T_c^2$	12.686	10.978

TABLE I. Input parameters and derived equilibrium and non-equilibrium quantities for our simulations. Our parameters are the effective number of relativistic degrees of freedom g_* , scalar potential parameters [see Eq. (6)] and nucleation temperature T_n . From these we obtain the latent heat \mathcal{L} , phase boundary tension σ and the thickness ℓ . For studying phase transitions, it is useful to also compute the equilibrium value of the scalar field at the nucleation temperature $\phi_b(T_n)$, transition strength parameters α_w and α_θ [see Eqs. (8) and (10)], the Chapman-Jouguet speed for detonations v_{CJ} , and the critical bubble radii R_c . Finally, we use Eq. (20) to compute a value for the Hubble constant H_n .

and the relativistic ideal fluid with 4-velocity U^μ . We use the techniques previously described in [21] (see also Refs. [38, 39], and the textbooks [40, 41]).

The field and fluid parts of the system are coupled together through a dissipative term that turns field stress-energy $T_\phi^{\mu\nu}$ into fluid stress-energy $T_f^{\mu\nu}$ such that,

$$\partial_\mu T_\phi^{\mu\nu} = -\eta U^\mu \partial_\mu \phi \partial^\nu \phi \quad (25)$$

where η is in general a function of ϕ and T with mass dimension 1. In previous work, including our own [20, 21], this was taken to be a constant. In this work we take $\eta = \tilde{\eta} \phi^2 / T$, where $\tilde{\eta}$ is a dimensionless parameter, which is better motivated by the underlying physics [42, 43]. The fluid velocity around the expanding bubbles for a given wall speed and phase transition strength is minimally affected by the change, as it is determined purely by hydrodynamics, except right at the bubble wall [32, 39, 44].

The parameters chosen in the numerical simulations are given in Table I. All dimensionful quantities are expressed in terms of the critical temperature T_c , defined from $\Delta V(T_c) = 0$.

We take the effective number of relativistic degrees of freedom to be the Standard Model's high temperature

value, although its exact value is not important³. The value of Newton’s constant G is arbitrary, as we will compute quantities which are independent of G .

We simulate at two different transition strengths, which we label “weak” ($\alpha \sim 10^{-2}$) and “intermediate” ($\alpha \sim 10^{-1}$). These have the same phase transition strengths as our “weak” and “intermediate” simulations in Refs. [20, 21], but the different form of the field-fluid coupling term, and the changed value of the relativistic degrees of freedom g_* mean that the simulations are not identical. The differences, however, are minor and do not affect the results.

For both weak and intermediate categories, we simulate at a variety of wall velocities giving both deflagrations and detonations, including some which move at close to the Chapman-Jouguet speed v_{CJ} , defined as the wall speed at which the exit velocity of the fluid in the wall frame is the speed of sound [36]. For a deflagration, $v_{\text{CJ}} = c_s$, while for a detonation it depends on the strength of the transition, but is always greater than c_s (see e.g. Ref. [32]). For a weak transition, $v_{\text{CJ}} \simeq c_s(1 + \sqrt{2\alpha\theta})$. Note that the values of the transition strength parameter in Table I, do not take into account the small increase in the temperature of the fluid near the moving bubble wall, and hence the stated Chapman-Jouguet speed is slightly higher than the true minimum speed of a detonation.

Each bubble is nucleated by inserting a scalar field configuration with Gaussian profile, as described in Ref. [21]. This profile is slightly larger than the critical bubble radius R_c . The bubble expands and perturbs the fluid, which evolves towards the scaling solution (c.f. Fig. 2).

Our bubbles are nucleated simultaneously, rather than with a physical nucleation rate. It is possible to rescale the results to yield the power spectrum from a more realistic nucleation rate. This was demonstrated in Ref. [15] and is discussed further in Section VI. We simulate with a variety of bubble numbers N_b , which controls the average bubble separation

$$R_* = (\mathcal{V}/N_b)^{\frac{1}{3}}. \quad (26)$$

After time t , each bubble is surrounded by a sound shell [22] of approximate thickness $\Delta R = \Delta v_w t$, where $\Delta v_w = |v_w - c_s|$.

For near-Jouguet bubble walls the sound shell is typically quite thin relative to the bubble separation. In the sound shell model [22], the velocity power spectrum peaks at $k\Delta R_* \sim 1$, where ΔR_* is the average bubble shell thickness at collision.

The bubble wall speeds and bubble separations are chosen to explore the dependence of the power spectra on R_* and ΔR_* , and also to compensate for the limited dynamic range of the simulations. The values of R_* and ΔR_* are listed in Table II.

In principle we need sufficiently large lattices to explore

$$dx \ll \ell \ll \Delta R_* \lesssim R_* \ll L_f. \quad (27)$$

In practice, the bubble wall does not need high resolution, as the detailed dynamics of the scalar field are not important beyond the transfer energy to the fluid. For the near-Jouguet transitions, we found it useful to explore the wavenumber range $kR_* \ll 1$ and $k\Delta R_* \gg 1$ separately by adjusting the number of bubbles. Simulations with large R_* have the advantage that the velocity field is closer to its asymptotic self-similar form.

Velocity and gravitational wave power spectra are computed on cubic periodic lattices with $N = 4200$ points per side. The lattice spacing dx , bubble number N_b , and bubble wall speed v_w , along with the field-fluid coupling required to obtain this speed, are listed in Table II.

We generally run with $dx = 2/T_c$ which has been established to work well for single bubble self-collisions for a weak deflagration and $R_* \approx 384/T_c$ [21].

Wall velocities v_w depend on discretisation effects, and it is difficult to determine the final asymptotic value from numerical simulations of limited duration. For concreteness, our quoted v_w values are determined from spherically symmetric simulations of a single bubble with $dxT_c = 0.2$ and are measured at time $5000/T_c$. For coarser lattice spacing the actual wall velocity will be slightly smaller, but the difference in the cases studied here is at most 3% (this effect is more pronounced for faster wall velocities [45]). In our simulations, the bubbles collide before the asymptotic profile is reached (see Fig. 2), and this is generally more significant than discretisation effects, particularly for simulations with smaller mean bubble separations.

For simulations with v_w close to c_s the lattice discretisation effects on the fluid profile were more significant than for other cases. In the weak, $v_w = 0.59$, $R_* \approx 1900/T_c$ case, we ran simulations at both $dx = 1/T_c$ and $dx = 2/T_c$ as a check against lattice effects in our final results. Agreement in the velocity power spectra is excellent until $kR_* \approx 100$, deteriorating to an error of about 50% at $kR_* \approx 200$. The discrepancy is more pronounced in the gravitational wave power spectrum because it convolves the power at different wavelengths [22].

IV. RESULTS: FLUID VELOCITY

In Fig. 1 we plot \bar{U}_f and \bar{U}_ϕ against time, showing the development, completion, and aftermath of the phase transition. We divide the transition into three phases [21]: the expansion phase before any bubble collisions take place, the collision phase, and the acoustic phase.

³ From Eq. (8) and the potential Eq. (6), one can see that the phase transition strength α_w can be kept constant if g_* , γ , A and λ are all scaled by some constant C . This will change the correlation length ℓ and hence the bubble wall thickness by a factor \sqrt{C} but will otherwise have little impact on the position or amplitude of the resulting gravitational wave power spectrum, so long as Eq. (27) holds.

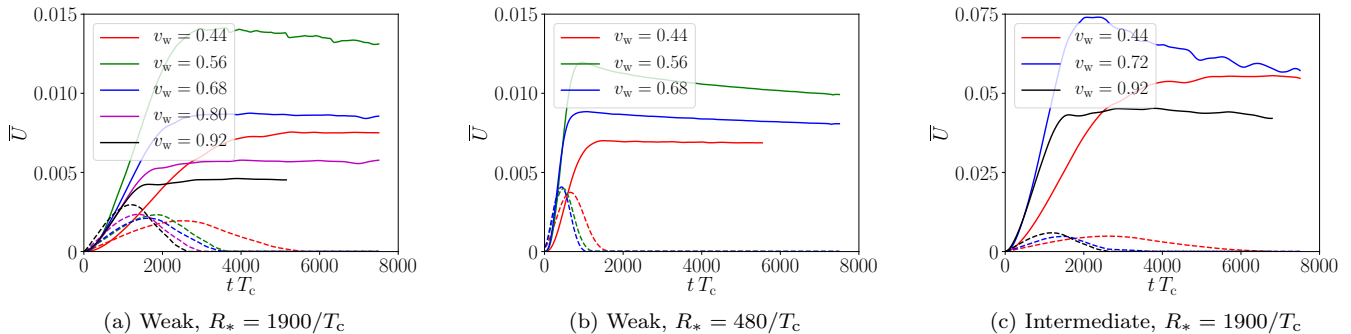


FIG. 1. RMS velocity and scalar gradient energy \overline{U}_f and \overline{U}_ϕ . Solid lines denote the RMS fluid velocity, dashed lines the RMS scalar field gradients.

Type	$\tilde{\eta}$	N_b	dxT_c	v_w	R_*T_c	ΔR_*T_c
Weak	0.19	84	2	0.92	1918	714.4
	0.35	84	2	0.80	1918	533.8
	0.51	84	2	0.68	1918	289.5
	0.59	11	1	0.56	1889	58.51
	0.93	84	2	0.44	1918	598.7
	0.51	5376	2	0.68	480	72.38
	0.59	5376	2	0.56	480	14.86
	0.93	5376	2	0.44	480	149.7
	Int.	0.17	84	2	0.92	1918
0.40		11	1	0.72	1889	374.2
0.62		84	2	0.44	1918	598.7

TABLE II. Simulation parameters $\tilde{\eta}$ (field-fluid coupling), N_b (number of bubbles nucleated) and lattice spacing dx , with the corresponding bubble wall speed v_w , mean bubble separation R_* and sound shell width $\Delta R_* = R_*|v_w - c_s|/c_s$. The potential parameters and derived quantities for the “weak” and “intermediate” phase transitions are given in Table I.

These can be traced in the Figures, using the fact that \overline{U}_ϕ^2 is proportional to the surface area of the phase boundaries. In the expansion phase, \overline{U}_ϕ grows linearly with time. In the collision phase, \overline{U}_ϕ falls below the initial linear behaviour, peaks, and drops to zero, marking the start of the acoustic phase. The RMS velocity \overline{U}_f also grows with \overline{U}_ϕ in the expansion and collision phase, and levels off in the acoustic phase. We take the peak of \overline{U}_ϕ to mark the collision time of the bubbles t_{pc} .

The RMS fluid velocity is generally constant in the acoustic phase, as noted in Ref. [21], although some reduction can be seen in the transitions with bubbles expanding at near the Chapman-Jouguet speed, where the fluid velocity profile is narrower and peaks at higher values (see deflagrations with $v_w = 0.56$ and detonations with $v_w \simeq 0.7$ in Fig. 2). It is possible that this reduction represents the beginning of turbulent transport of energy to the lattice dissipation scale; the time for shocks and turbulence to appear is in these cases $\tau_{sh} \sim 10^5/T_c$, only

a factor of order 10 longer than the simulation time.

Fig. 2 also shows how the fluid profiles evolve as the bubbles expand. The profile takes some time to settle to its asymptotic self-similar form, and we plot both this, and the profile at the peak collision time t_{pc} . The difference is particularly noticeable for small bubble separations where collisions happen much earlier (see Fig. 2b); the fluid profiles are smooth and do not have the characteristic sharp edges at the wall position. This affects the high wavenumber behaviour of the velocity power spectra, as we shall see.

In Table III we list the maximum RMS fluid velocity \overline{U}_f^{\max} , along with the transverse component $\overline{U}_{f,\perp}^{\max}$. We also give theoretical values for the mean square fluid velocity estimated in two ways. Firstly, $\overline{U}_f^{\text{1D}}$ is obtained by integrating the numerical 1D fluid profiles out to $t = 7000/T_c$, according to (see Refs. [21, 32])

$$\left(\overline{U}_f^{\text{1D}}\right)^2 = \frac{3}{v_w^3} \int d\xi \xi^2 W^2 v^2, \quad (28)$$

where $\xi = r/t$ is the scaled radius, $v(\xi)$ is the radial fluid velocity and $W(\xi)$ the associated fluid gamma factor.

The second estimate is $\overline{U}_f^{\text{Esp}} = \sqrt{\frac{3}{4}\kappa_v\alpha}$, where the function $\kappa_v(v_w, \alpha)$ given in the Appendix of Espinosa et al. [32], using v_w extracted from 1D simulations at $t = 7000/T_c$, and $\alpha = \alpha_\theta(T_n)$ from Table I. Note that κ_v is defined from the trace of the spatial part of the energy-momentum tensor as

$$\kappa_v\alpha_\theta = \frac{1}{\epsilon\mathcal{V}} \int d^3x \tau_f^{ii}. \quad (29)$$

We see that the rotational component of the velocity field is very small, consistent with the interpretation of the fluid flow as sound waves, and with the linearity of the flow. We also see that the Espinosa et al. [32] fitting formula for the mean square fluid velocity around a single bubble gives a good estimate of the mean square velocity of the 3D flow. Finally, the time at which the scalar gradient energy peaks is approximately $t_{pc} \simeq 0.6R_*/v_w$

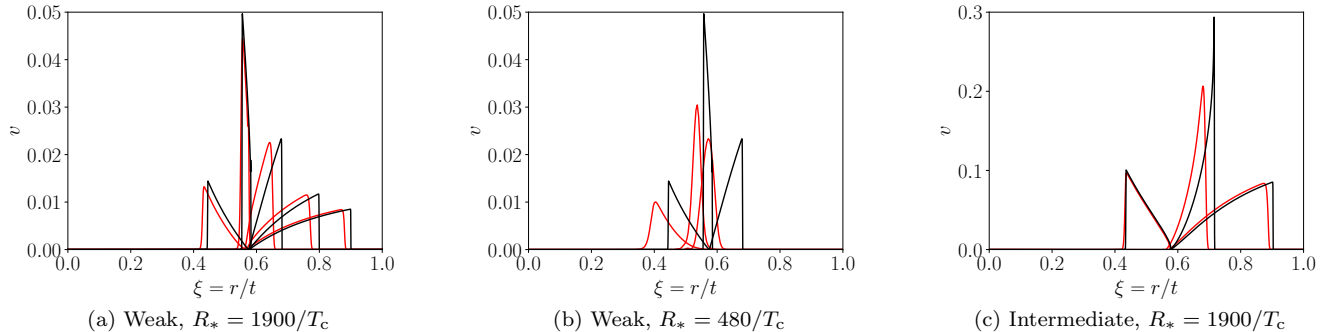


FIG. 2. Fluid radial velocity profiles as a function of scaled radius $\xi = r/t$. In red are curves taken at the peak of \bar{U}_ϕ (see Fig. 1), at times t_{pc} given in Table III. In black are fluid velocities at late times, $t \gtrsim 10000/T_c$. Note that the wall speeds can be read off from the positions of the phase transition fronts. Although the v_w quoted in the main text comes from simulations with a smaller lattice spacing ($dxT_c = 0.2$), the discrepancy is small – at most 3% for the fastest detonations.

Type	v_w	R_*T_c	$t_{pc}T_c$	$10^3\bar{U}_f^{\max}$	$10^3\bar{U}_{f,\perp}^{\max}$	$10^3\bar{U}_f^{1D}$	$10^3\bar{U}_f^{\text{Esp}}$
Weak	0.92	1918	1210	4.60	0.0833	5.31	5.32
	0.80	1918	1380	5.75	0.0665	6.39	6.50
	0.68	1918	1630	8.65	0.116	9.17	10.0
	0.56	1889	1860	13.8	0.190	14.3	14.7
	0.44	1918	2520	7.51	0.0775	7.70	7.76
	0.68	480	430	8.74	0.252	9.17	10.0
	0.56	480	480	11.7	0.498	14.3	14.7
	0.44	480	660	6.99	0.131	7.70	7.76
Int.	0.92	1918	1180	43.7	0.869	51.6	53.7
	0.72	1889	1480	65.0	1.97	72.8	95.0
	0.44	1918	2650	54.5	2.77	51.7	67.7

TABLE III. Wall speed v_w , average bubble separation R_* , with peak bubble collision time t_{pc} , the maximum fluid RMS velocity \bar{U}_f^{\max} , the maximum contribution of transverse fluid motion $\bar{U}_{f,\perp}^{\max}$, and two estimates for \bar{U}_f based on 1D fluid profiles and a fitting formula given in Ref. [32].

in the simulations with R_* is large. This is consistent with interpreting this peak as a bubble collision time.

In Figs. 3, 4 and 5 we plot velocity power spectra (15) for a set of simulations. We divide the data according to the bubble wall speed v_w , separating out the special case of deflagrations moving at close to sound speed.

In Fig. 3 we show detonations with wall speeds $v_w = 0.92$, 0.80 and $v_w \simeq 0.7$ for transitions of weak and intermediate strength. The intermediate strength transition at $v_w = 0.72$ is run at a higher resolution ($dx = 1/T_c$) to resolve the higher velocity gradients, so that the mean bubble separation ($1889/T_c$) is close to the box size of the simulation ($2100/T_c$), hence there is less dynamic range on the long-wavelength side of the peak in the power spectrum.

The general form is a broken power law, with a domed peak at $kR_* = O(10)$. The shape is similar between the weak and intermediate cases at the same velocity; the

intermediate strength transitions have higher amplitude, as more energy is transferred into kinetic energy. This is in accord with the sound shell model [22], where the velocity power spectra are of a universal shape for a given wall velocity and non-relativistic fluid flows with negligible shocks.

The width of the dome is larger for the detonations with wall speeds closer to the speed of sound, with the peak displaced to the right relative to the fast detonation. This is also consistent with the sound shell model prediction that the peak position in the power spectrum is determined by the inverse width of the sound shell.

The power-law to the right of the dome is close to the k^{-1} predicted by the sound shell model, particularly in the detonations, where there is a clear separation between the peak scale and the wall width scale. The long-wavelength power law index is not so clear, as there are few bins and there are fewer k vectors in each bin, but is consistent with the predicted k^3 .

In Fig. 4 we show velocity power spectra from deflagrations with wall speed $v_w = 0.44$. The power law to the right of the dome appears steeper than the k^{-3} prediction, and there is a knee in the power spectrum at higher k neither of which is in accord with the sound shell model. These features need further investigation.

We recall that in the sound shell model, there are two scales in the velocity field: the mean bubble separation R_* , and the sound shell width $\Delta R_* = R_*\Delta v_w/v_w$. If the scales are well separated (i.e. if the bubble wall is moving close to the speed of sound), the long-wavelength k^3 power law is predicted to turn into a k^1 power law at $kR_* = O(1)$, and finally to a k^{-1} power law at $k\Delta R_* = O(1)$.

The clearest scale separation should be found in transitions where the wall speed is closest to the sound speed. In Fig. 5 we show the power spectra from a deflagration with speed $v_w = 0.56$, very close to $c_s = 1/\sqrt{3} \simeq 0.577$.

We do not have the dynamic range to resolve all three wavelength ranges simultaneously, but by altering the

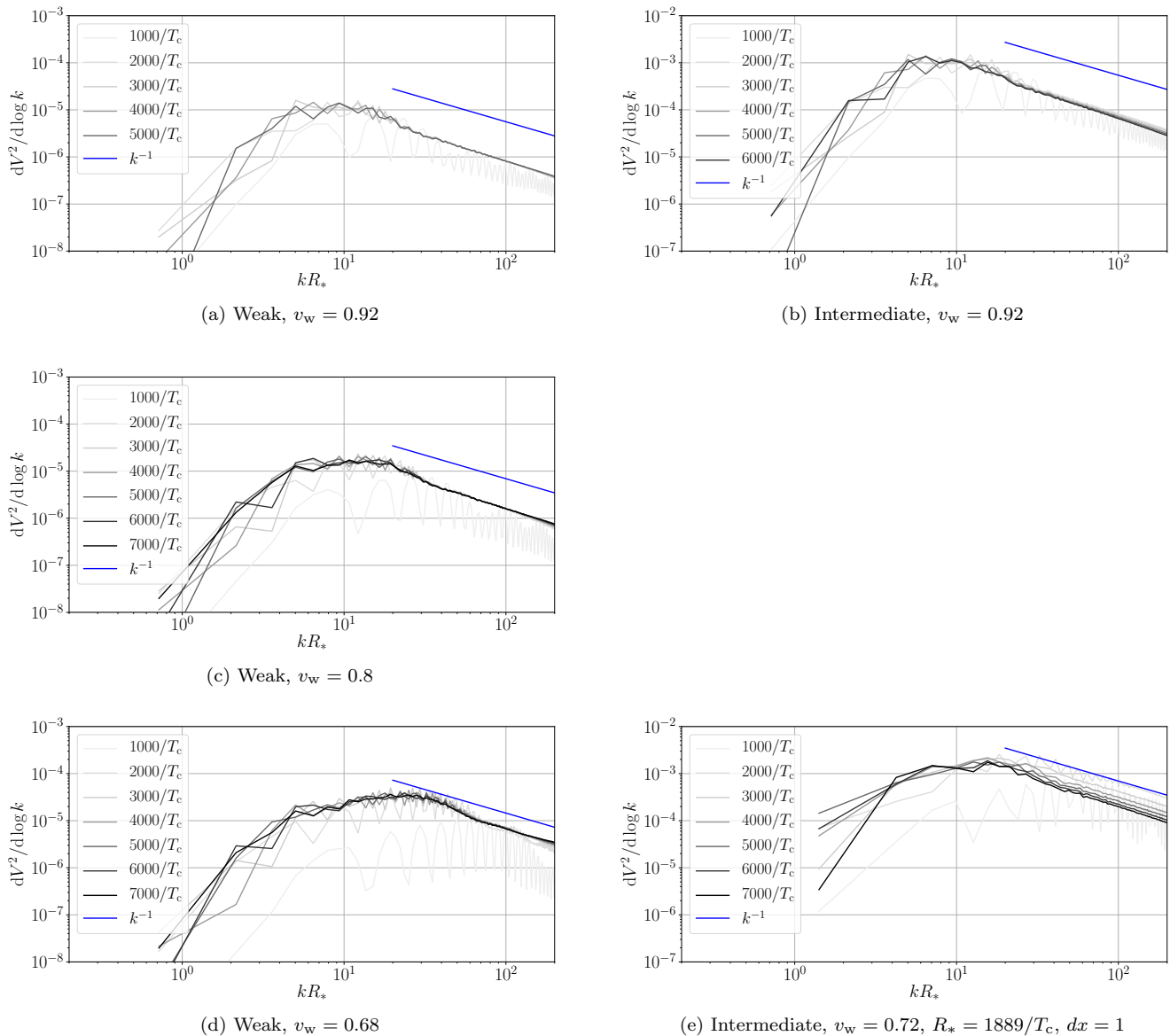


FIG. 3. Velocity power spectra for detonations. Left are weak strength phase transitions, with $v_w = 0.92, 0.80$ and 0.68 . Right are intermediate phase transitions, with $v_w = 0.92$ and $v_w = 0.72$. All have $N_b = 84$ bubbles (average separation $R_c = 1918/T_c$) and a lattice spacing $dx = 2/T_c$, with the exception of the $v_w = 0.72$ intermediate transition which has $N_b = 11$ ($R_* = 1889/T_c$) and $dx = 1/T_c$. Note there is no intermediate strength transition with $v_w = 0.80$.

number of bubbles we can try to resolve two ranges at a time. At the top, for the largest R_* , we see that the dome around the peak has broadened into a slowly rising plateau, consistent with a k^1 behaviour. At higher wavenumber the plateau drops off, although we do not have enough range to confirm a k^{-1} behaviour.

For larger numbers of bubbles (centre, bottom in Fig. 5) the long-distance behaviour emerges. With $N_b = 5376$ ($R_* = 480/T_c$) one can clearly see a steep power law, even steeper than k^3 , in the range $1 \lesssim kR_* \lesssim 3$. A possible reason for the discrepancy with the generic sound shell model prediction at low kR_* is that the coefficient of the k^3 term is proportional to $\Delta v_w^2 \simeq 4 \times 10^{-4}$ [22], and

so the next order term in a series expansion in kR_* can dominate for $kR_* = O(1)$. The short-distance behaviour at these large bubble numbers is not reliable, as there is insufficient distinction between the sound shell width $\Delta R_* \simeq 15/T_c$ and the bubble wall width $\ell \simeq 3/T_c$. Indeed, in Fig. 2 one can see that the fluid velocity profiles are far from their asymptotic forms.

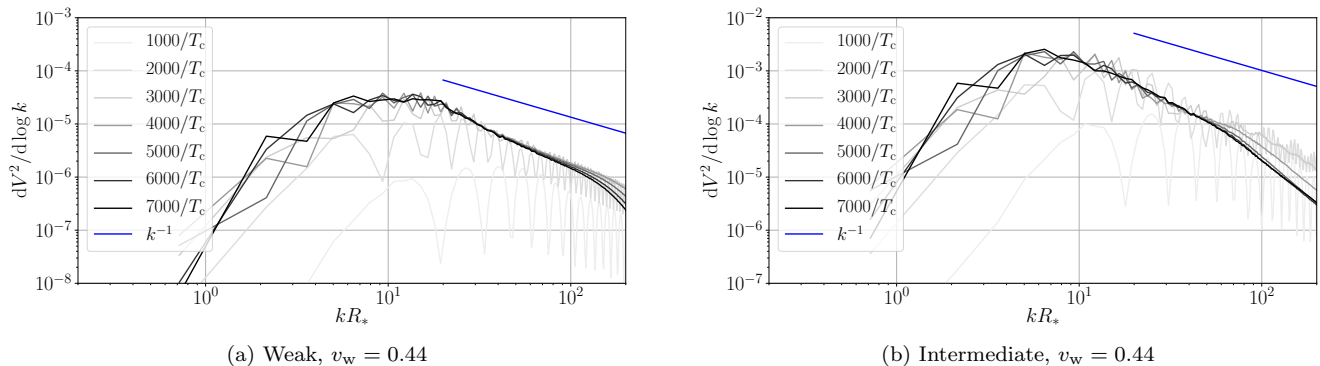


FIG. 4. Velocity power spectra for deflagrations with $v_w = 0.44$. Left is a weak phase transition, right is an intermediate transition. Both have $N_b = 84$ bubbles (mean separation $R_c = 1918/T_c$).

Type	v_w	R_*T_c	$\xi_f^{\text{end}}T_c$	$\xi_{\text{gw}}^{\text{end}}T_c$	$10^2\tilde{\Omega}_{\text{gw}}^{\xi_f}$	$10^2\tilde{\Omega}_{\text{gw}}^{R_*}$
Weak	0.92	1918	1490	1620	1.5	1.2
	0.80	1918	1290	1600	2.2	1.4
	0.68	1918	888	1410	1.5	0.62
	0.56	1889	530	865	1.4	0.32
	0.44	1918	1450	1750	1.4	1.1
	0.68	480	268	323	1.5	0.88
Int.	0.56	480	233	416	1.6	0.86
	0.44	480	416	493	1.5	1.3
	0.92	1918	1530	1780	2.6	2.0
	0.72	1889	1100	1180	3.3	1.8
	0.44	1918	1980	2090	1.6	1.7

TABLE IV. Wall speed v_w and mean bubble separation R_* , with the resulting integral scale of the fluid flow ξ_f^{end} , the integral scale of the gravitational wave power $\xi_{\text{gw}}^{\text{end}}$, and the dimensionless gravitational wave amplitude parameters $\tilde{\Omega}_{\text{gw}}^{\xi_f}$ and $\tilde{\Omega}_{\text{gw}}^{R_*}$.

V. RESULTS: GRAVITATIONAL WAVES

In Table IV we show global quantities computed from the gravitational wave power spectrum

$$\tilde{\mathcal{P}}_{\text{gw}}(z) = \frac{z^3}{2\pi^2} \tilde{P}_{\text{gw}}(z), \quad (30)$$

where $z = kR_*$. These are the integral scale of the gravitational waves

$$\xi_{\text{gw}} = \frac{1}{\Omega_{\text{gw}}} \int \frac{dk}{k} \frac{1}{k} \frac{d\Omega_{\text{gw}}}{d\ln(k)}, \quad (31)$$

calculated at the end of the simulations, and the dimensionless gravitational wave amplitude parameter defined in (24), with the fluid length scale L_f is taken to be either the integral scale of the velocity field ξ_f (defined analogously to Eq. 31) or the mean bubble separation R_* . With either of these length scales, $\tilde{\Omega}_{\text{gw}}$ is approxi-

mately constant and of order 10^{-2} for weak transitions.⁴ The integral scales of both the fluid and the gravitational waves are significantly smaller for the near-Jouguet transitions, showing the influence of the sound shell thickness.

In Figs. 6 to 8 we plot power spectra of the fractional energy density in gravitational waves. The spectra are divided by the mean bubble separation R_* and the time t in units of the Hubble distance and time, and plotted against wavenumber in units of the inverse bubble separation, for ease of comparison with Eq. (21). Taking the fluid flow length scale to be R_* , we have

$$\frac{1}{(H_n t)(H_n R_*)} \frac{d\Omega_{\text{gw}}(k)}{d\ln(k)} = 3\Gamma^2 \bar{U}_f^4 \tilde{\mathcal{P}}_{\text{gw}}(kR_*). \quad (32)$$

Note that by dividing by time, gravitational wave power generated in the collision phase will decrease, while acoustic phase gravitational wave power will asymptote to a constant. Note also that, by dividing by H_n^2 , we arrive at a quantity which is independent of G .

One can see that, at late times, the shape of the power spectrum appears to change little, and is settling down to a characteristic shape. We would expect power laws to be less clear in the gravitational wave power spectrum than in the velocity power spectrum, as the former is a convolution of the latter over a range $\Delta k = \pm c_s k$ at wavenumber k [21].

Where power laws are established over a sufficient range, we expect that the a velocity power spectrum going as k^n should produce a gravitational wave power spectrum going as k^{2n-1} . The sound shell model [22] predicts $n = -1$ for $R_*/\Delta R_* \ll kR_* \ll R_*/\ell$, $n = 1$ for $1 \ll kR_* \ll R_*/\Delta R_*$ (if the scales R_* and ΔR_* are well separated), and $n = 3$ for $kR_* \ll 1$.

In Fig. 6 we show the gravitational wave power spectra from detonations ($v_w = 0.92$, 0.80 , and $v_w \simeq 0.7$)

⁴ Note that there is a numerical error in the computation of $\tilde{\Omega}_{\text{gw}}$ in [21] which resulted in a value which was a factor $(2\pi)^3/32\pi$ too high.

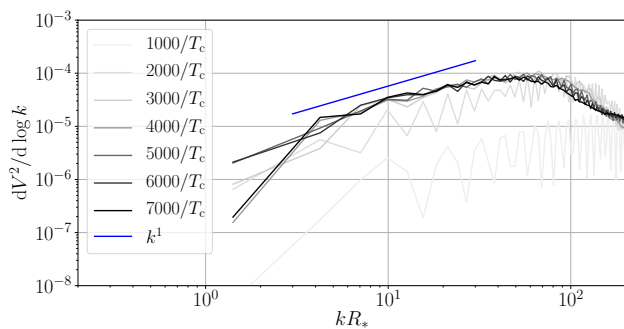
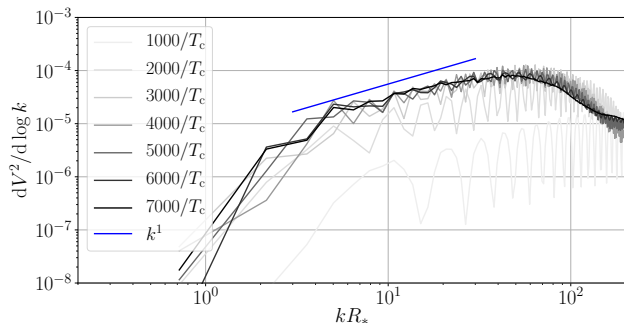
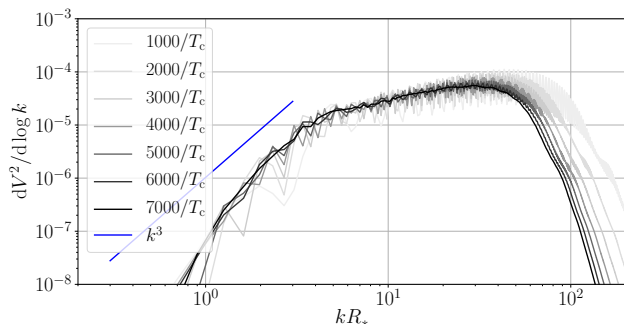
(a) $N_b = 11$, $dx = 1$ (b) $N_b = 84$ (c) $N_b = 5376$

FIG. 5. Velocity power spectra for near-Jouguet deflagrations. All are weak transitions with $v_w = 0.56$, and $N_b = 11, 84$ and 5376 ($R_c = 1889/T_c, 1918/T_c,$ and $480/T_c$).

for transitions of weak and intermediate strength, arising from the velocity fields with power spectra in Fig. 3. Again, the general form is a broken power law, with a domed peak at $kR_* = O(10)$. As with the velocity power spectrum, the shape is similar between the weak and intermediate cases at the same wall velocity; the intermediate strength transitions have higher amplitude, resulting from the higher RMS velocity. We see that the broader dome in the velocity power spectrum translates to a broader feature in the gravitational wave spectrum, although the features around the peak are not well resolved, particularly in the intermediate strength transition.

The power-law to the right of the dome is close to the k^{-3} predicted by the sound shell model, particularly in the detonations. The predicted k^5 power law at long-wavelengths is difficult to discern, as it is buried under a feature established during the collision phase.

In Fig. 7 we show gravitational wave power spectra from a deflagration with $v_w = 0.44$, for weak and intermediate strength transitions. The power law at high k is steeper than k^{-3} , inconsistent with the sound shell model, but are consistent with velocity power spectra steeper than k^{-1} .

In Fig. 8 we show the gravitational wave power spectra from a deflagration with speed $v_w = 0.56$, where the sound shell is very thin, and there are clearly two scales in the power spectra. Again, the low- k behaviour is hidden behind the gravitational waves from the collision phase due to the limited duration of the simulation, although there is a suggestion of a steepening below $kR_* \sim 5$ in the case with the maximum long-wavelength resolution, $N_b = 5376$. It is clear that the peak is at around $kR_* \simeq 50$, which is understandable in terms of the scale $k\Delta R_* \simeq 2$.

VI. MODELLING THE POWER SPECTRUM FOR LISA

Our simulations nucleate all bubbles simultaneously, whereas in a real thermal phase transition away from metastability, the nucleation rate rises exponentially as $p(t) = p_0 \exp[\beta(t - t_f)]$ after the temperature drops below the critical temperature, where β is the transition rate parameter, and t_f is the time at which the volume fraction of the symmetric phase is $1/e$ [30]. This means that there are a few larger, bubbles earlier in the transitions, and more smaller bubbles as the transition ends. Numerical experiments with the gravitational wave power spectrum in the envelope approximation [15] show that the principal effect of instantaneous nucleation for a given mean bubble separation is to increase the peak frequency by a factor of approximately 1.7, and decrease the amplitude by a factor of about 3. The shape of the power spectrum is not significantly changed. This rescaling can be regarded as a rescaling of the relationship between the mean bubble separation R_* and the transition rate parameter β .

We shall assume that the same is true for the velocity field generated by the colliding bubbles, i.e. that the shape is not significantly changed by using a realistic nucleation history, and that the principal effect is to change the proportionality constant in the standard relation $R_* = (8\pi)^{1/2} v_w / \beta$ [30]. With this assumption we can directly use our measured power spectra as models for the gravitational wave power spectrum from a phase transition.

In the LISA Cosmology Working Group report [8] the acoustic gravitational wave power spectrum was mod-

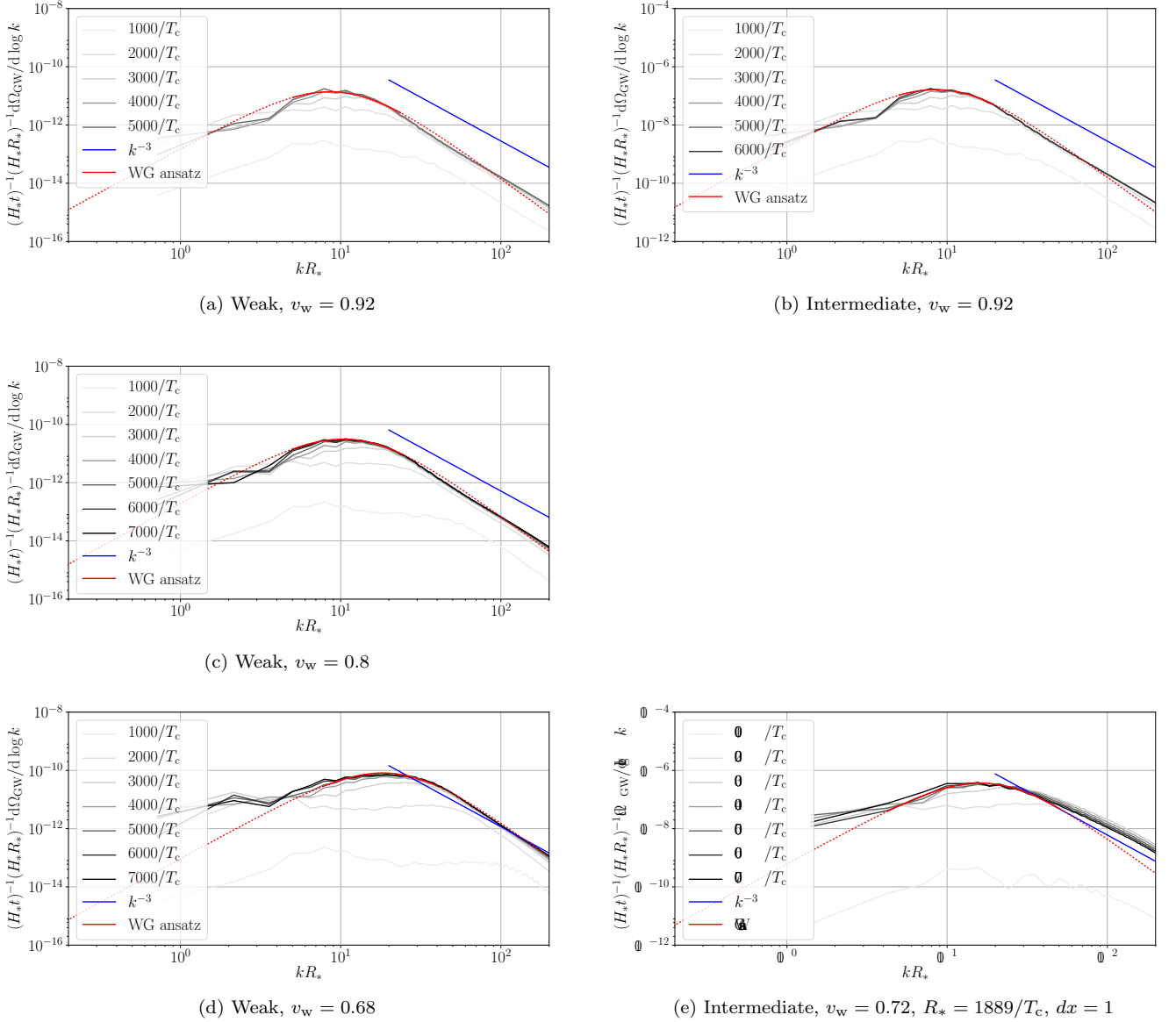


FIG. 6. Power spectra of fractional energy density in gravitational waves for detonations, divided by the ratio of the mean bubble separation R_* to the Hubble length at the transition H_n , and the ratio of the time to the Hubble time. The wave number is scaled by the mean bubble separation. Left are weak phase transitions, showing detonations with $v_w = 0.92$, 0.80 and 0.68 (top to bottom). Right are intermediate phase transitions, with wall speeds $v_w = 0.92$ and $v_w = 0.72$. All have $N_b = 84$ bubbles, giving a mean bubble separation of $R_* = 1918/T_c$, and a lattice spacing $dx = 2/T_c$, with the exception of the $v_w = 0.72$ intermediate transition which has $N_b = 11$ ($R_* = 1889/T_c$) and $dx = 1/T_c$.

elled using a broken power law function:

$$\frac{d\Omega_{\text{gw}}(k)}{d\ln(k)} = (H_n R_*) AC(s) \quad (33)$$

where

$$C(s) = s^3 \left(\frac{7}{4 + 3s^2} \right)^{7/2}, \quad (34)$$

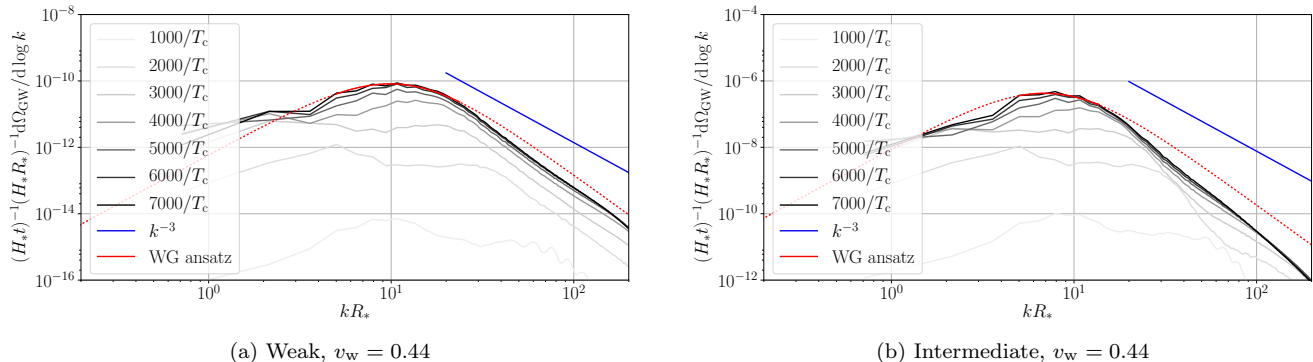
and

$$s = \frac{kR_*}{(kR_*)_{\text{max}}}. \quad (35)$$

The dimensionless parameters A and $(kR_*)_{\text{max}}$ determine the magnitude and the location of the maximum of the power spectrum, respectively. The form of the function is motivated by the results from hydrodynamical gravitational wave production simulations in ref. [21]. The power spectrum of the ansatz at small k is $\propto k^3$, turning over to $\propto k^{-4}$ at large k .

The detailed structure of the ansatz determines the width of the dome between the small- k and large- k regions; indeed, the width of the dome can be adjusted by

FIG. 7. Power spectra of fractional energy density in gravitational waves for deflagrations with $v_w = 0.44$, divided by the ratio of the mean bubble separation R_* to the Hubble length at the transition H_n , and the ratio of the time to the Hubble time. The wave number is scaled by the mean bubble separation. Left is a weak phase transition, right is an intermediate transition. Both have $v_w = 0.44$ and $N_b = 84$ ($R_* = 1918/T_c$).



Type	v_w	R_*	$(kR_*)_{\max}$	A	A_{est}
Weak	0.92	1918	8.6	1.4×10^{-11}	1.9×10^{-11}
	0.80	1918	10.4	3.1×10^{-11}	5.9×10^{-11}
	0.68	1918	18.3	8.1×10^{-11}	14×10^{-11}
	0.44	1918	9.9	8.2×10^{-11}	12×10^{-11}
Int.	0.92	1918	8.5	1.6×10^{-7}	2.7×10^{-7}
	0.72	1889	16.1	3.7×10^{-7}	13×10^{-7}
	0.44	1918	6.9	4.3×10^{-7}	5.3×10^{-7}

TABLE V. The fit parameters of the ansatz (33). $(kR_*)_{\max}$ is the location of the maximum of the power spectrum, and A its amplitude, along with the estimate from Eq. (37).

generalising the ansatz to a form

$$C_a(s) = s^3 \left(\frac{7}{4 + 3s^a} \right)^{7/a}. \quad (36)$$

In order to enable direct comparison with the working group results we fit the measured power spectrum using the original ansatz (33).

The resulting fits are shown as dashed lines in Fig. 6 for detonations and in Fig. 7 for deflagrations, and fit parameters are listed in Table V. The functions are fitted only in the neighbourhood of the domes, but at least for the weak detonations the fitted functions describe the overall behaviour of the data surprisingly well.

By integrating (33) and comparing to Eq. (23), we can derive an estimate for the amplitude parameter from our simulations,

$$A_{\text{est}} \simeq 0.687 \Gamma^2 \bar{U}_f^4 \tilde{\Omega}_{\text{gw}}^{R_*}. \quad (37)$$

The estimates, computing from the values of \bar{U}_f in Table III and $\tilde{\Omega}_{\text{gw}}^{R_*}$ in Table IV, are shown in the last column of Table V.

It can be seen that the amplitude estimates based on numerical integration of the scaled gravitational wave

power spectrum $\tilde{\mathcal{P}}_{\text{gw}}$ are generally higher than those derived from the fit: this is because the numerical power spectrum exaggerates the low- k part of the power spectrum derived from the collision phase. In the case of the intermediate strength transition at $v_w = 0.72$, the dome is less apparent, and the fitting formula underpredicts the gravitational wave spectrum at high k . We recommend using the fitting formula for wall velocities away from the Chapman-Jouguet speed by about $|v_w - v_{\text{CJ}}| \gtrsim 0.1$.

For the near-Jouguet deflagration ($v_w = 0.56$) the dome in the power spectrum becomes very broad, as can be seen in Fig. 8. In this case the fit ansatz (33) cannot describe the behaviour well. It is possible to construct more complicated fit functions which can capture the structure at intermediate scales, but the limited numerical data makes it difficult to see universal features. We leave the detailed analysis of the Jouguet case for further analysis.

The peak angular frequency in units of the mean bubble separation $z_p = (kR_*)_{\max}$ is generally around 10, except near the Chapman-Jouguet speed where it is larger. Qualitatively this agrees with the estimate for the peak frequency made in ref. [8] $f_p \simeq 1.2\beta/v_w$, with the phase transition rate parameter $\beta \simeq 3v_w/R_*$. For a more precise estimate we must take into account the fact that nucleating bubbles simultaneously changes the effective transition rate for a given R_* [15], as outlined above. A power spectrum peaking at $(kR_*) = z_p$ in our simulations corresponds to a true peak frequency

$$f_p \simeq \frac{0.54}{S} \frac{\beta}{v_w} \frac{z_p}{10}. \quad (38)$$

where $S \simeq 2$ is a factor which takes into account the overestimate of the frequency for a given R_* .

In order calculate the observed frequency of waves emitted with frequency f_p (38) at time t_n when the Hubble parameter was H_n , we note that the peak frequency

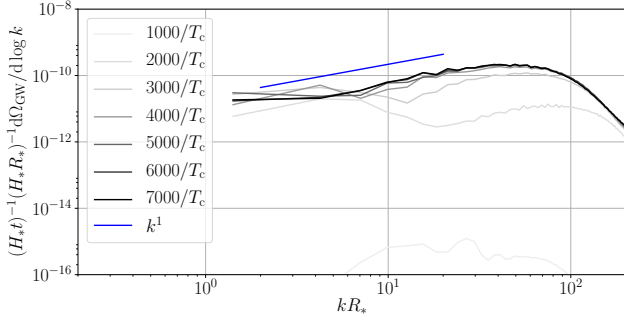
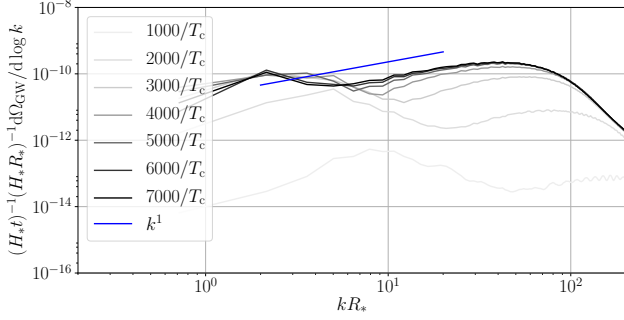
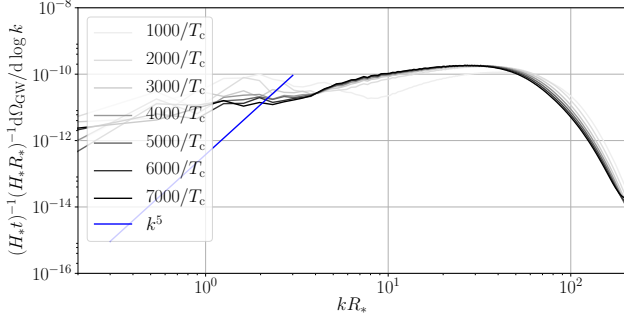
(c) $N_b = 11$, $dx = 1$ (d) $N_b = 84$ (e) $N_b = 5376$

FIG. 8. Power spectra of fractional energy density in gravitational waves for near-Jouguet deflagrations, $v_w = 0.56$, divided by the ratio of the mean bubble separation R_* to the Hubble length at the transition H_n , and the ratio of the time to the Hubble time. The wave number is scaled by the mean bubble separation. All are weak transitions with $N_b = 11, 84$ and 5376 ($R_* = 1889/T_c, 1918/T_c,$ and $480/T_c$).

today can be written

$$f_{p,0} = \frac{f_p}{H_n} H_{n,0}, \quad (39)$$

Here

$$H_{n,0} = 16.5 \left(\frac{T_n}{10^2 \text{ GeV}} \right) \left(\frac{h_*}{100} \right)^{\frac{1}{6}} \mu\text{Hz} \quad (40)$$

is the Hubble rate at the nucleation temperature, redshifted to today, assuming that the dominant source of

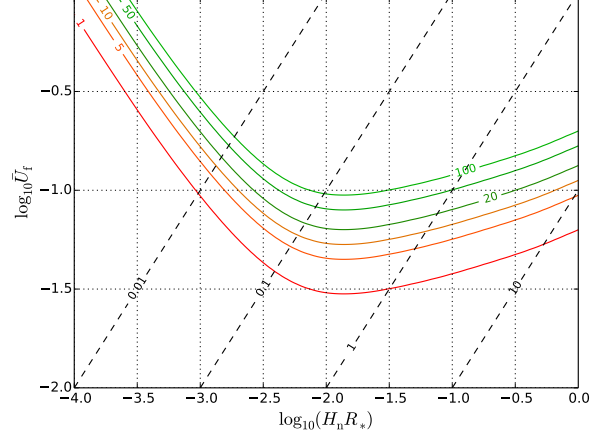


FIG. 9. Signal-to-noise ratio (solid contours) for the model power spectrum (33), using our acoustic peak gravitational wave power estimate (37), with eLISA configuration described in the text, and taking the nucleation temperature to be $T_n = 100$ GeV. Dashed lines show the ratio of the order of magnitude of the shock appearance timescale $R_* H_n / \bar{U}_f$. For ratios of order 1 the fluid flow can be assumed to be purely acoustic, while for values much less than 1, the fluid flow may become turbulent within a Hubble time, and further investigation is required.

energy density is radiation. Hence

$$f_{p,0} \simeq 26 \left(\frac{1}{H_n R_*} \right) \left(\frac{z_p}{10} \right) \left(\frac{T_n}{10^2 \text{ GeV}} \right) \left(\frac{h_*}{100} \right)^{\frac{1}{6}} \mu\text{Hz}, \quad (41)$$

To obtain the amplitude of the gravitational wave power spectra today, the power spectrum (21) and total power (23) must be multiplied by a factor $F_{\text{gw},0} = \Omega_{\gamma,0}(h_0/h_*)^{\frac{1}{3}}(h_0/2)$, where $\Omega_{\gamma,0}$ is the density parameter of photons today, h_0 is the effective number of relativistic degrees of freedom contributing to the entropy today, and $h_* \simeq g_*$ is the corresponding number at the time of gravitational wave generation.

Using the Planck best-fit value $H_0 = 67.8 \pm 0.9 \text{ km s}^{-1} \text{ Mpc}^{-1}$ [46], and the FIRAS temperature for the CMB $T_{\gamma,0} = 2.725 \pm 0.002 \text{ K}$ [47], we have

$$F_{\text{gw},0} = (3.57 \pm 0.05) \times 10^{-5} \left(\frac{100}{h_*} \right)^{\frac{1}{3}}. \quad (42)$$

Our final expression for the acoustic gravitational wave power spectrum today is

$$\frac{d\Omega_{\text{gw},0}}{d\ln(f)} = 0.68 F_{\text{gw},0} \Gamma^2 \bar{U}_f^4 (H_n R_*) \tilde{\Omega}_{\text{gw}} C \left(\frac{f}{f_{p,0}} \right). \quad (43)$$

In Fig. 9 we show the signal-to-noise ratio expected at a LISA-like gravitational wave observatory with 6 laser links of arm length 2 Gm and a 5-year mission duration [48] (intermediate between configurations C1 and

C2 of the eLISA Cosmology Working Group report [8]). The SNR is shown as contours in the $(\bar{U}_f, H_n R_*)$ plane, for a phase transition with a reference temperature of $T_n = 100$ GeV, and taking $\tilde{\Omega}_{\text{gw}} = 1.2 \times 10^{-1}$. This value reproduces the peak amplitude for the intermediate strength transition with $v_w = 0.92$. It under-predicts the power spectrum for the intermediate strength transition at other wall speeds we simulated, and is therefore a conservative estimate.

We also show contours of $R_* H_n / \bar{U}_f$, which gives the timescale for the appearance of shocks relative to the Hubble time. We do not expect the acoustic gravitational wave power spectrum to be an accurate description for $R_* H_n / \bar{U}_f \ll 1$.

From the figure, we can conclude that, for a phase transition at 100 GeV, LISA's peak sensitivity will be towards transitions with mean bubble separation of about a hundredth the Hubble length, at which scale an intermediate strength deflagration or detonation ($\bar{U}_f \simeq 5 \times 10^{-2}$) should produce a SNR of around 10, taken as the detection threshold in [8]. However, this is also in the region where one cannot safely assume that the fluid has not developed shocks. Further simulations are required for a more accurate determination of LISA's ability to explore the parameter space of phase transitions.

VII. CONCLUSIONS

We have performed the largest numerical simulations to date of first order phase transitions in the early universe, and computed the resulting fluid velocity and gravitational wave spectra for a range of bubble wall speeds v_w , mean bubble separations R_* , and transition strengths α_w . The power spectra are more tightly pinned down than in our previous campaign of simulations [21].

We observe a gravitational wave power spectrum with a rising power law, a broad dome at $kR_* = O(10)$, and a decreasing power law at higher k . The dome widens to a slowly rising plateau for bubble wall speeds close to the speed of sound.

In the case of detonations the spectra exhibit a k^{-3} power law in good agreement with the sound shell model [22], but the high- k power law for deflagrations appears slightly steeper.

We establish that there are two length scales in the gravitational wave power spectrum: besides the mean bubble separation R_* there is also the mean sound shell thickness $\Delta R_* = R_* \Delta v_w / c_s$. For a thin sound shell, where $\Delta R_* \ll R_*$, the slowly rising plateau has a power law consistent with the k^1 predicted by the sound shell model.

We do not have sufficient computational volume to determine the gravitational wave power spectrum at $kR_* \lesssim O(1)$, but the velocity power spectra for generic wall speeds are consistent with k^3 there, which should lead to k^5 in the gravitational waves. In the special case of a just-subsonic deflagration, where the sound shell is very

thin, the velocity power spectrum is steeper than k^3 for $kR_* \lesssim O(1)$. This is not in contradiction with the sound shell model, which only gives k^3 for $kR_* \lesssim O(|v_w - c_s|)$.

Our simulations are still not large enough to properly resolve all the different wavenumber regimes simultaneously, and they reveal an interesting knee in the velocity power spectra for deflagrations at high k . This feature appears to be established at about the peak bubble collision time t_{pc} , where the area of the phase boundary is at its maximum. Yet larger simulations are therefore needed to resolve the full power spectrum, and a separate simulation campaign to investigate the deflagration power spectra.

We also need to run the simulations for longer, with larger fluid velocities, in order to investigate the transition to turbulence. Flows with larger fluid velocities become turbulent earlier, and are likely to be important for the gravitational wave signals observable by LISA.

However, for transitions which are weak enough that turbulence does not develop, and have bubble wall speeds not too close to the speed of sound, we are confident in the form of the power spectrum, and offer the fitting formula (33) for the gravitational wave power spectrum. This can safely be used for RMS fluid velocities up to $\bar{U}_f \lesssim R_* H_n$, or $\kappa_v \alpha_\theta \lesssim (H_n / \beta)^2$ in terms of the kinetic energy conversion efficiency κ_v and the transition strength parameter α_θ (see Eq. 29).

Using the fitting formula, we computed the signal-to-noise ratio at a LISA-like mission with 6 laser links, arm length 2 Gm, and a duration of 5 years. At a transition temperature of $T_n = 100$ GeV, we find that such a mission has greatest sensitivity to transitions with mean bubble separation is about 10^{-2} of the Hubble length. At this bubble separation, LISA will be able to detect the signal from phase transitions down to latent heat to energy ratio $\alpha_w \simeq 0.1$, i.e. intermediate strength in our terminology.

We also checked the timescale for the development of shocks and turbulence, finding that a significant fraction of the detectable parameter space is in a region where one cannot safely assume that the fluid flow remains linear. Further simulations are required to examine the transition to turbulence, necessary for a more accurate determination of LISA's ability to explore the parameter space of phase transitions.

There is a range of extensions of the standard model (SM), which could produce a gravitational wave signal in reach of LISA [8]. Most of these models are extensions of the SM Higgs sector by additional scalar fields, principally SU(2) singlets or doublets, or modifications of the SM Higgs potential itself. Furthermore, LISA could also probe phase transitions in the TeV range, e.g. possible confinement transitions in strong coupling completions of the electroweak theory.

A strong phase transition in these models can either come from 1) a modified zero temperature Higgs potential, as is often the case in singlet extensions, or 2) additional thermal contributions to the Higgs potential, or 3)

a combination of both, as e.g. in the Two-Higgs-Doublet model. Models of type 2) and 3) will show a stronger dependence of the nucleation rate on temperature (via the energy of the critical bubble), which results in a smaller value of β/H . So models of type 1) will have large bubbles at fixed α compared to types 2) and 3). As a result models of type 1) may show a stronger gravitational wave signal without reaching the state of turbulence.

Most of the models will show an observable gravitational wave signal only when the walls propagate as fast detonations, but there may be exceptions as has been shown e.g. for the 2HDM [49].

More generally, the fact that the shape of the gravitational wave power spectrum depends on the bubble wall speed means that it could become possible to determine v_w from a detection of the stochastic gravitational wave background with sufficiently high signal-to-noise ratio.

Delineating the ability of future space-based gravitational wave detectors to constrain the full set of phase transition parameters α , β , v_w and T_n of an electroweak-scale first order transition, thereby opening a new quantitative window onto physics beyond the Standard Model, is now an important goal.

ACKNOWLEDGMENTS

The LISA Cosmology Working Group has provided an important forum for discussing our work and we thank

its members as well as its coordinators, Chiara Caprini and Germano Nardini. We owe a huge debt also to the late Pierre Binétruy for his work on cosmological sources of gravitational waves, his work with LISA, and in particular his encouragement of our work.

We acknowledge PRACE for awarding us access to resource HAZEL HEN based in Germany at the High Performance Computing Center Stuttgart (HLRS). Our work was supported by the Munich Institute for Astro- and Particle Physics (MIAPP) of the DFG cluster of excellence “Origin and Structure of the Universe”.

MH (ORCID ID 0000-0002-9307-437X) and SH acknowledge support from the Science and Technology Facilities Council (grant number ST/L000504/1). KR (ORCID ID 0000-0003-2266-4716) is supported by the Academy of Finland grant 267286. DJW (ORCID ID 0000-0001-6986-0517) was supported by the People Programme (Marie Skłodowska-Curie actions) of the European Union Seventh Framework Programme (FP7/2007-2013) under grant agreement number PIEF-GA-2013-629425.

-
- [1] B. P. Abbott et al. (Virgo, LIGO Scientific), *Phys. Rev. Lett.* **116**, 061102 (2016), arXiv:1602.03837 [gr-qc].
 - [2] B. P. Abbott et al. (Virgo, LIGO Scientific), *Phys. Rev. Lett.* **116**, 241103 (2016), arXiv:1606.04855 [gr-qc].
 - [3] N. Bartolo et al., *JCAP* **1612**, 026 (2016), arXiv:1610.06481 [astro-ph.CO].
 - [4] S. A. Sanidas, R. A. Battye, and B. W. Stappers, *Phys. Rev.* **D85**, 122003 (2012), arXiv:1201.2419 [astro-ph.CO].
 - [5] S. A. Sanidas, R. A. Battye, and B. W. Stappers, *Astrophys. J.* **764**, 108 (2013), arXiv:1211.5042 [astro-ph.CO].
 - [6] J. Aasi et al. (VIRGO, LIGO Scientific), *Phys. Rev. Lett.* **112**, 131101 (2014), arXiv:1310.2384 [gr-qc].
 - [7] J. J. Blanco-Pillado, K. D. Olum, and B. Shlaer, *Phys. Rev.* **D89**, 023512 (2014), arXiv:1309.6637 [astro-ph.CO].
 - [8] C. Caprini et al., *JCAP* **1604**, 001 (2016), arXiv:1512.06239 [astro-ph.CO].
 - [9] H. Audley et al., (2017), arXiv:1702.00786 [astro-ph.IM].
 - [10] M. Armano et al., *Phys. Rev. Lett.* **116**, 231101 (2016).
 - [11] A. Kosowsky, M. S. Turner, and R. Watkins, *Phys. Rev.* **D45**, 4514 (1992).
 - [12] A. Kosowsky, M. S. Turner, and R. Watkins, *Phys. Rev. Lett.* **69**, 2026 (1992).
 - [13] M. Kamionkowski, A. Kosowsky, and M. S. Turner, *Phys. Rev.* **D49**, 2837 (1994), arXiv:astro-ph/9310044 [astro-ph].
 - [14] S. J. Huber and T. Konstandin, *JCAP* **0809**, 022 (2008), arXiv:0806.1828 [hep-ph].
 - [15] D. J. Weir, *Phys. Rev.* **D93**, 124037 (2016), arXiv:1604.08429 [astro-ph.CO].
 - [16] R. Jinno and M. Takimoto, *Phys. Rev.* **D95**, 024009 (2017), arXiv:1605.01403 [astro-ph.CO].
 - [17] D. Bodeker and G. D. Moore, *JCAP* **0905**, 009 (2009), arXiv:0903.4099 [hep-ph].
 - [18] D. Bodeker and G. D. Moore, (2017), arXiv:1703.08215 [hep-ph].
 - [19] C. J. Hogan, *MNRAS* **218**, 629 (1986).
 - [20] M. Hindmarsh, S. J. Huber, K. Rummukainen, and D. J. Weir, *Phys. Rev. Lett.* **112**, 041301 (2014), arXiv:1304.2433 [hep-ph].
 - [21] M. Hindmarsh, S. J. Huber, K. Rummukainen, and D. J. Weir, *Phys. Rev.* **D92**, 123009 (2015), arXiv:1504.03291 [astro-ph.CO].
 - [22] M. Hindmarsh, (2016), arXiv:1608.04735 [astro-ph.CO].
 - [23] A. Kosowsky, A. Mack, and T. Kahniashvili, *Phys. Rev.* **D66**, 024030 (2002), arXiv:astro-ph/0111483 [astro-ph].
 - [24] A. Nicolis, *Class. Quant. Grav.* **21**, L27 (2004), arXiv:gr-qc/0303084 [gr-qc].
 - [25] C. Caprini and R. Durrer, *Phys. Rev.* **D74**, 063521 (2006), arXiv:astro-ph/0603476 [astro-ph].
 - [26] C. Caprini, R. Durrer, and G. Servant, *JCAP* **0912**, 024 (2009), arXiv:0909.0622 [astro-ph.CO].
 - [27] T. Kahniashvili, L. Kisslinger, and T. Stevens,

- Phys. Rev. **D81**, 023004 (2010), arXiv:0905.0643 [astro-ph.CO].
- [28] T. Kahniashvili, A. Brandenburg, L. Campanelli, B. Ratra, and A. G. Tevzadze, Phys. Rev. **D86**, 103005 (2012), arXiv:1206.2428 [astro-ph.CO].
- [29] L. Kisslinger and T. Kahniashvili, Phys. Rev. **D92**, 043006 (2015), arXiv:1505.03680 [astro-ph.CO].
- [30] K. Enqvist, J. Ignatius, K. Kajantie, and K. Rummukainen, Phys.Rev. **D45**, 3415 (1992).
- [31] J. Ignatius, K. Kajantie, H. Kurki-Suonio, and M. Laine, Phys.Rev. **D49**, 3854 (1994), arXiv:astro-ph/9309059 [astro-ph].
- [32] J. R. Espinosa, T. Konstandin, J. M. No, and G. Servant, JCAP **1006**, 028 (2010), arXiv:1004.4187 [hep-ph].
- [33] C. Caprini, R. Durrer, T. Konstandin, and G. Servant, Phys.Rev. **D79**, 083519 (2009), arXiv:0901.1661 [astro-ph.CO].
- [34] D. G. Figueroa, M. Hindmarsh, and J. Urrestilla, Phys. Rev. Lett. **110**, **101302** (2013), arXiv:1212.5458 [astro-ph.CO].
- [35] A. Brandenburg, K. Enqvist, and P. Olesen, Phys. Rev. **D54**, 1291 (1996), arXiv:astro-ph/9602031 [astro-ph].
- [36] L. D. Landau and E. M. Lifshitz, Fluid Mechanics, 2nd ed., Course of Theoretical Physics, Vol. 6 (Butterworth-Heinemann, 1987).
- [37] U.-L. Pen and N. Turok, Phys. Rev. Lett. **117**, 131301 (2016), arXiv:1510.02985 [astro-ph.CO].
- [38] H. Kurki-Suonio and M. Laine, Phys.Rev. **D51**, 5431 (1995), arXiv:hep-ph/9501216 [hep-ph].
- [39] H. Kurki-Suonio and M. Laine, Phys.Rev. **D54**, 7163 (1996), arXiv:hep-ph/9512202 [hep-ph].
- [40] J. Wilson and G. Matthews, Relativistic Numerical Hydrodynamics (Cambridge University Press, Cambridge, 2003).
- [41] L. Rezzolla and O. Zanotti, Relativistic Hydrodynamics, EBSCO ebook academic collection (OUP Oxford, 2013).
- [42] G. D. Moore and T. Prokopec, Phys.Rev. **D52**, 7182 (1995), arXiv:hep-ph/9506475 [hep-ph].
- [43] S. J. Huber and M. Sopena, (2013), arXiv:1302.1044 [hep-ph].
- [44] P. J. Steinhardt, Phys.Rev. **D25**, 2074 (1982).
- [45] D. Cutting, private communication (2017).
- [46] P. A. R. Ade et al. (Planck), Astron. Astrophys. **594**, A13 (2016), arXiv:1502.01589 [astro-ph.CO].
- [47] J. C. Mather, D. J. Fixsen, R. A. Shafer, C. Mosier, and D. T. Wilkinson, Astrophys. J. **512**, 511 (1999), arXiv:astro-ph/9810373 [astro-ph].
- [48] A. Klein et al., Phys. Rev. **D93**, 024003 (2016), arXiv:1511.05581 [gr-qc].
- [49] G. C. Dorsch, S. J. Huber, T. Konstandin, and J. M. No, (2016), arXiv:1611.05874 [hep-ph].